

Experimental and computational comparison of freeze–thaw induced pressure generation in red and sugar maple

Maryam Zarrinderakht^a, Isabell Konrad^b, Timothy R. Wilmot^c, Timothy D. Perkins^c,
Abby van den Berg^c, John M. Stockie^{d,*}

^a*Department of Earth, Ocean and Atmospheric Sciences, University of British Columbia, 2207 Main Mall, Vancouver, BC, V6T 1Z4, Canada*

^b*Comsysto Reply GmbH, Tumblingerstraße 23, 80337 Munich, Germany*

^c*Proctor Maple Research Center, University of Vermont, 58 Harvey Road, Underhill, Vermont, 05489, USA*

^d*Department of Mathematics, Simon Fraser University, 8888 University Drive, Burnaby, BC, V5A 1S6, Canada*

Abstract

Sap exudation refers to the process whereby trees such as sugar (*Acer saccharum*) and red maple (*Acer rubrum*) generate unusually high positive stem pressure in response to repeated cycles of freeze and thaw. This elevated xylem pressure permits the sweet sap to be harvested over a period of several weeks and hence is a major factor in the viability of the maple syrup industry. The extensive literature on sap exudation documents various competing hypotheses regarding the physical and biological mechanisms driving positive pressure generation in maple, but to date relatively little effort has been expended on devising detailed mathematical models for the exudation process. In this paper, we utilize an existing model of Graf et al. [J. Roy. Soc. Interface 12:20150665, 2015] that describes heat and mass transport within the multiphase gas–liquid–ice mixture within the porous xylem tissue. The model captures the inherent multiscale nature of xylem transport by including phase change and osmotic transport within wood cells on the microscale, which is coupled to heat transport through the tree stem on the macroscale. We extend this model by incorporating a root reflection coefficient that introduces an asymmetry in root water flux and hence permits a more realistic accumulation of stem pressure. A parametric study based on simulations with synthetic temperature data singles out the essential model parameters that have greatest impact on stem pressure build-up. Measured daily temperature fluctuations are then used as model inputs and the resulting simulated pressures are compared directly with experimental measurements taken from mature red and sugar maple stems during the sap harvest season. The results demonstrate that our multiscale freeze–thaw model reproduces realistic exudation behavior, thereby providing novel insights into the specific physical mechanisms that dominate positive pressure generation in maple trees.

Keywords: exudation pressure, xylem transport, red and sugar maple, tree sap, freeze–thaw mechanism, multiscale modelling

1. Introduction

Both sugar maple (*Acer saccharum*) and red maple (*Acer rubrum*) have a remarkable ability to generate positive xylem (or sapwood) pressure in response to freeze–thaw cycles, during a season

*Corresponding author (jstockie@sfu.ca)

when the tree is leafless and mostly dormant. The resulting exudation pressure can persist on and off for weeks or even months, which allows maple sap to be harvested in sufficient quantities that it is an economically viable agricultural product in northeastern North America. A few other tree species such as black walnut (*Juglans nigra*), butternut (*Juglans cinerea*) and white birch (*Betula papyrifera*) are likewise capable of generating significant exudation pressures, but none to such a high degree as maple. It is well-known that the presence of dissolved sugar (1% or more by mass) in the sap of these species plays an important role in the accumulation of stem pressure during the freeze–thaw process (Marvin, 1968), but the precise causes of sap exudation have proven difficult to pinpoint. Indeed, exudation has been studied extensively for over 150 years, during which time researchers have attributed it to a wide variety of physical and biological mechanisms, including osmosis (Wiegand, 1906); thermal expansion of gas, water and wood (Sachs, 1860; Merwin and Lyon, 1909; Marvin, 1949); cryostatic suction (Stevens and Eggert, 1945); and active processes in living cells (Johnson, 1945; Marvin, 1958).

A major advance in the understanding of exudation was achieved by Milburn and O’Malley (1984), whose experimental observations inspired them to propose a purely physical hypothesis for maple sap exudation based on a freeze–thaw mechanism that incorporates distinctive features of the cellular structure of maple wood. More specifically, their model focused on two classes of cells in the maple xylem: libriform fibers that are filled with gas and are considered to play mainly a structural role; and vessels and tracheids that are mostly liquid-filled and constitute the primary pathways for sap transport. Milburn and O’Malley’s breakthrough came from recognizing that during a freezing cycle, liquid is drawn into the normally gas-filled fibers by cryostatic suction thereby freezing on the interior surface of fiber walls and compressing the gas trapped within. During a subsequent thaw, the stored pressure is released into the vessel sap. This model certainly explains how sap pressure can be stored and released during a sequence of freeze–thaw events, however it remains incomplete owing to its failure to explain the essential role of dissolved sugars which are known to play a major role in exudation.

This gap in understanding was addressed by Tyree (1995) who recognized that one consequence of the sugar content in sap is to suppress the natural tendency in gas–liquid suspensions for gas bubbles to dissolve at high pressure. He proposed a modification of the Milburn–O’Malley model that incorporates two additional physical effects: expansion, contraction and dissolution of gas bubbles in response to pressure variations in the suspending fluid; and existence of an osmotic potential due to differences in solute concentration engendered by the selectively permeable nature of certain cell walls in maple xylem. In particular, Tyree argued that the lignified walls separating fiber and vessel permit water and small solutes to pass but impede larger molecules like sucrose that make up the bulk of solutes in maple sap. This gives rise to a significant osmotic potential between vessels (containing high-sucrose sap) and surrounding fibers (containing pure water). Tyree then demonstrated that this osmotic potential is sufficient to stabilize gas bubbles over long enough time periods to sustain a realistic exudation pressure, and the role of the selectively permeable fiber/vessel walls in osmosis was later confirmed experimentally by Cirelli et al. (2008). An extensive review of the current literature on positive stem pressure and its causes can be found in the paper by Schenk et al. (2021).

Despite these advances in understanding of physical mechanisms behind pressure generation in sugar maple and related species, significant controversy remains in the literature over the causes of exudation. For example, Améglio et al. (2001) argued that “no existing single model explains all of the winter xylem pressure data” supported by experiments suggesting that biological processes in living wood cells are necessary for exudation. These differences in opinion have been exacerbated

by the lack of a mathematical description for the exudation process. Indeed, around the time that Milburn and O’Malley developed their model, Tyree (1983) commented that “there is insufficient quantitative information to set up a system of physical equations to describe the model”. Some efforts have since been made to formulate equations governing certain aspects of the relevant physics, such as the diffusion model for embolism recovery developed by Yang and Tyree (1992) that captures the gas transport and dissolution processes similar to that which occurs in exudation.

However, it was only in a series of papers (Ceseri and Stockie, 2013, 2014; Graf and Stockie, 2014; Graf et al., 2015) that a concerted attempt was made to devise a complete mathematical model of the essential physical mechanism behind the freeze–thaw process of Milburn and O’Malley (1984), modified to include the influence of suspended gas bubbles and osmotic pressure (Tyree, 1995; Cirelli et al., 2008). The model is based on a system of nonlinear diffusion equations for the cellular scale freeze–thaw process that incorporate sap phase change, compression and dissolution of gas bubbles, and osmosis (Ceseri and Stockie, 2013, 2014), and captures the pressure exchange between fibers and vessels during a single freeze–thaw cycle. This cellular-level model was then coupled with a macroscale heat transport equation obtained by a multi-scale averaging process known as periodic homogenization (Graf et al., 2015). Numerical simulations yielded realistic pressure oscillations as well as a build-up in exudation pressure over multiple freeze–thaw cycles. These homogenized model simulations were then compared with laboratory experiments on black walnut trees subjected to an imposed periodic variation in temperature (Améglio et al., 2001) and exhibited excellent qualitative agreement. A recent paper by Reid et al. (2020) compared experimental measurements of maple stem temperatures with solutions to a simpler but closely-related model of heat transfer only, and demonstrated the effectiveness of this class of models in predicting realistic stem temperatures.

In this paper we extend the homogenized exudation model of Graf et al. (2015) by incorporating a root reflection coefficient that embodies the differential in root conductivity between inflow and outflow, which is essential for capturing realistic positive stem pressures. Our main aim is to validate the model using experimental measurements consisting of temperature and pressure time-series sampled over a period of roughly 40 days from red and sugar maple trees located at the University of Vermont Proctor Maple Research Center in Underhill, Vermont, USA. Having such a highly-resolved dataset provides an ideal opportunity to validate the time-dependent model for maple sap exudation under actual field conditions.

After describing the experimental procedures used to collect field measurements on maple trees in Section 2 we present the multiscale sap exudation model in Section 3, which states the primary simplifying assumptions and supplies sufficient details to elucidate the essential physical processes underlying the model. The comparison of experimental and numerical results in Sections 4–5 begins with a parameter sensitivity analysis for a model tree subjected to a synthetic (smoothly-varying) ambient temperature, which aims to determine best estimates for parameters used in our simulations of real maple trees. We then perform a sequence of simulations using actual temperature data that feature rapid variations and significant levels of noise. A detailed comparison is then drawn between stem pressures from simulations and experiments in order to validate our hypothesis that a multiscale model based solely on physical transport processes is capable of reproducing realistic exudation pressures in maple trees subjected to repeated cycles of freeze and thaw.

2. Materials and Methods: Field Experiments

Measurements were taken during the spring sap flow season over the years 2005–2010 in several mature sugar maple and red maple trees ranging in size from 14 to 61 cm DBH (diameter at breast



Figure 1: Photograph of a taphole containing a black nylon spout that is connected by plastic tubing to an Omega PX-26-030GV pressure sensor. Additional wires leading to thermocouples are also shown.

height). The trees were located 180 m within the experimental sugarbush to the southeast of the laboratory of the University of Vermont Proctor Maple Research Center in Underhill, Vermont, at approximately 425 m elevation. Type-T (24-gauge) thermocouples were used to measure the following: air temperature at heights of 1.2 m and 16.5 m; branch temperature measured in the center of a hole drilled in a canopy branch at 16.5 m height, and within the tapping zone at 1.2 m height and 5 cm depth; and soil temperature at depths of 0 cm (surface) and 30 cm. Pressure measurements were made by drilling a standard 1.1 cm diameter, 5 cm deep taphole and inserting a black nylon maple spout in an inverted position. A tube leading from the spout was filled with water and connected to an Omega PX-26-030GV pressure sensor (with $\pm 1\%$ accuracy). Both thermocouples and pressure sensors were wired to a Campbell Scientific 21X datalogger and measurements were stored at 15 minute intervals. A photograph showing the taphole and wired connections is given in Figure 1. Stem temperature and pressure were measured on both north and south sides of the tree and were often very divergent. Sap flow was measured from a taphole in a similarly-sized tree nearby using a standard maple spout connected via tubing to a collection chamber. A pressure sensor in the bottom was used to convert pressure to depth, so that exuded sap volume and flow rate could be determined for each interval. Data were downloaded from the datalogger as comma-separated values and stored in Excel files for analysis.

3. Materials and Methods: Mathematical Model

3.1. Background on xylem structure in maple

Before presenting the mathematical model for the freeze–thaw process governing sap exudation, we begin by briefly summarizing the physical and structural characteristics of maple xylem that play an essential role in sap transport and exudation (more detail is provided in Tyree and Zimmermann (2002)). The xylem in hardwood trees such as maple is made primarily of rigid and nearly cylindrical structures that consist of the hollowed-out walls of dead wood cells. Sapwood has a regular and quasi-periodic microstructure shown in Figure 2a that consists of regularly spaced vessels

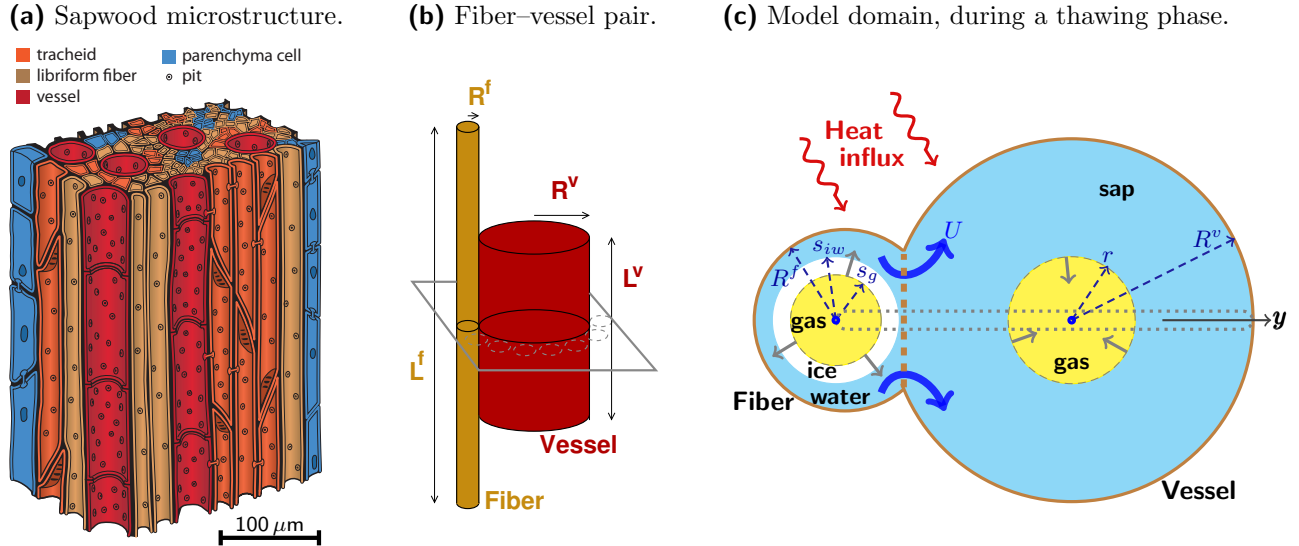


Figure 2: Sapwood microstructure and the idealized 2D model geometry. (a) A microscopic cut-away view of the sapwood within a typical hardwood tree, depicting the vessels and (libriform) fibers that are central to the model. Tracheids are connected hydraulically to neighbouring vessels via paired pits, which is why they are “lumped together” in our model with vessels. Note that fiber walls also contain pits, but they are unpaired and hence unconnected to adjacent vessels or tracheids. (b) A single fiber–vessel pair showing the main geometric parameters. The horizontal cutting plane highlights the planar cross-section corresponding to the 2D model geometry in Figure 2c. The dashed circles represent the N copies of the fiber that are incorporated into the equations through a simple multiplier N . (c) The 2D model geometry depicting a thawing scenario. A thawing fiber of radius R^f (containing nested layers of gas, ice and liquid water) is located adjacent to a thawed vessel of radius R^v (containing gas and liquid sap). As the fiber ice layer thaws, the fiber gas bubble expands and forces melt-water through the porous wall into the vessel at a rate U , thereby compressing the vessel gas and increasing the vessel sap pressure.

interspersed with much more abundant tracheids and (libriform) fibers having a smaller diameter. Vessels are the primary water-conducting conduits in sapwood, and each is divided lengthwise into vessel elements that are connected end-to-end via perforation plates, thereby forming long capillary tubes. Vessel walls are interspersed with cavities called pits that connect cells hydraulically through pit membranes as long as the pits in adjacent cells align or “pair up”. Tracheids are intermediate in size between vessels and fibers and are also connected through paired pits with neighbouring vessels and other tracheids. Since both vessels and tracheids are mostly sap-filled, they serve as the primary conduits for xylem sap transport. Fibers on the other hand are known to contain mostly gas (Milburn and O’Malley, 1984) and their walls demonstrate a relative lack of pitting. As a result, they are usually regarded to have negligible impact on sap transport and instead serve a structural function. The lignified fiber walls have nonetheless been found to contain micropores (much smaller than those in pit membranes) which are selectively permeable, allowing water and small solutes to pass but inhibiting the passage of larger molecules like sucrose (Cirelli et al., 2008).

3.2. Microscale model for the thawing process

We next describe our model for the essential processes governing sap exudation on the microscopic (cellular) scale which include: heat transport; phase change due to freezing and thawing; expansion, contraction and dissolution of gas; and porous flow through pit membranes and selectively-permeable micropores in the fiber–vessel wall. Our ultimate goal is to model repeated

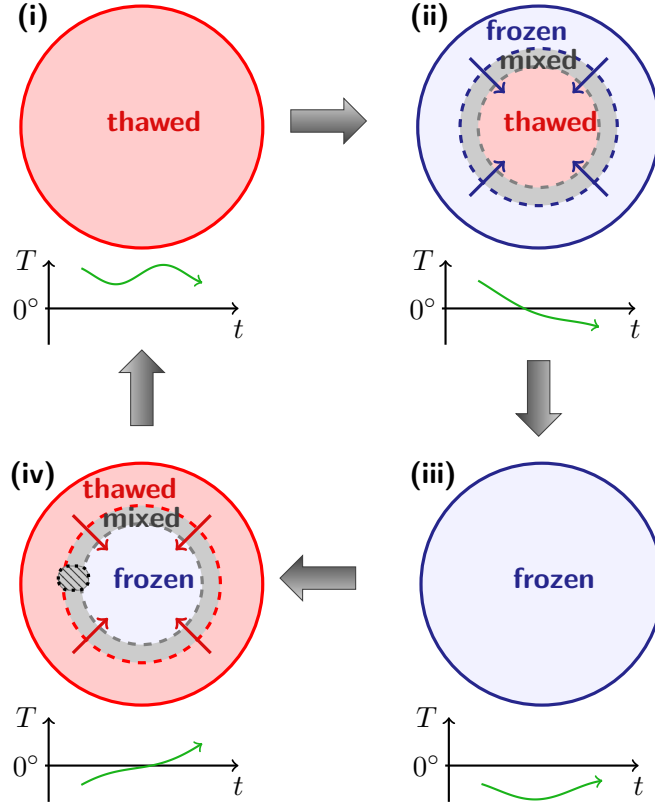


Figure 3: The freeze–thaw process within a circular tree stem cycles between four main phases ($i \rightarrow ii \rightarrow iii \rightarrow iv \rightarrow i \rightarrow \dots$) as ambient temperature T cycles below and above the freezing point: (i) completely thawed (with $T > 0$); (ii) partially frozen ($T \searrow 0$), with a freezing front advancing radially inward to the center of the stem; (iii) completely frozen ($T < 0$); (iv) partially thawed ($T \nearrow 0$), with a thawing front advancing radially inward. The freezing/thawing fronts in (ii,iv) are thin annular regions (shaded in grey, and in reality much thinner than depicted here) wherein the liquid is in a “mixed” state; that is, the water in the fibers is freezing/frozen and the sap in the vessels thawing/thawed. The thawing front circled on the left of (iv) is magnified in Figure 2c to the cellular scale, which depicts an individual vessel and an adjacent fiber in a partially thawed state.

freeze–thaw cycles in response to ambient temperature variations as depicted in Figure 3, where a thawing (or freezing) front propagates into the tree stem and separates regions of the sapwood that are frozen from those that are thawed. The front actually comprises a thin annular section of sapwood that exists in a mixed state containing water/sap in both liquid and ice forms. We focus our attention on equations for the thawing process only and refer the interested reader to Graf et al. (2015) for the modifications required to capture all other possible freeze–thaw states.

In order to derive a model that is tractable, we make a number of simplifying assumptions:

- A1. Vertical variations due to gravity and height-dependence are neglected, so that we can focus on a 2D horizontal cross-section through a circular tree stem.
- A2. At the cellular level, we consider only the contribution of vessels and fibers to exudation. Tracheids are not treated separately but rather lumped together with vessels. Other sapwood components (such as ray cells) are ignored.
- A3. Sapwood has a uniform, periodic microstructure consisting of cylindrical vessels and fibers,

both having constant lengths (L^v, L^f) and radii (R^v, R^f). Then we can reasonably restrict our attention to a horizontal slice through a single vessel element and adjacent fiber as pictured in Figure 2b.

- A4. Each vessel is in contact with N fibers on average (see Figure 2b) so that the influence of multiple fibers can be incorporated by simply multiplying by a factor of N the contribution from the single fiber being modelled.
- A5. Based on the circular symmetry of the fiber and vessel, we take all microscopic variables to depend on a radial coordinate y passing through the fiber and vessel centers.
- A6. Gas is also present in the vessels, which is consistent with observations showing that exuding maple sap contains suspended gas bubbles (Wiegand, 1906; Marvin and Greene, 1959; Perkins and van den Berg, 2009). Because water and sap are incompressible fluids, we must include some gas in the vessel to facilitate pressure exchange between fiber and vessel.
- A7. Gas, liquid and ice within the fiber and vessel exist as distinct layers arranged in concentric annuli as shown in Figure 2c. This is consistent with Milburn and O'Malley (1984) who conjectured that ice accumulates on the inner fiber wall due to cryostatic suction from previous freezing cycles to encase a central gas bubble, and that during a thawing cycle any liquid melt-water collects in a layer between the ice and the wall.
- A8. The temperature in the gas and ice layers is assumed to be constant and equal to that of the adjacent liquid. Furthermore, during any freeze or thaw cycle the temperatures of the gas/ice layers in the fiber remain constant at the critical temperature T_c . This is justified because the fiber radius is roughly 6 times smaller than in the vessel, and the thermal diffusivities for gas and ice are so much larger than that for liquid (Tyree and Zimmermann, 2002).
- A9. Any liquid entering the fiber from the vessel must be pure water owing to the selective permeability of the fiber–vessel wall (Cirelli et al., 2008).
- A10. Liquid water is present within the soil even under freezing conditions and tree roots actively transport water throughout the entire freeze–thaw cycle, both of which are supported by observations (Marvin, 1958; Robitaille et al., 1995; Sorkin, 2014).

Based on the above assumptions, we now present the governing equations for the thawing phase of the exudation cycle in which vessel are thawed and fibers are still partially frozen (depicted in Figure 2c and corresponding to phase (iv) in Figure 3). Full details of the derivation can be found in Ceseri and Stockie (2013); Graf et al. (2015). The physical state of the various phases within a given vessel and fiber can be described by the following six time-dependent functions:

$s_g(t)$: fiber gas bubble radius, measured from the center of the fiber,

$s_{iw}(t)$: radius of the fiber ice-water interface,

$r(t)$: vessel gas bubble radius,

$U(t)$: total volume of melt-water that flows through the porous fiber–vessel wall, measured positive from fiber to vessel,

$U_r(t)$: total volume of soil water influx through the roots,

$\mathcal{T}(y, t)$: temperature in the vessel sap, which also depends on the radial coordinate y with origin at the vessel center so that $r(t) \leq y \leq R^v$ (recall that temperature is taken to be constant elsewhere in the fiber and vessel).

We will now state equations for the first five unknowns, leaving the microscale heat equation for \mathcal{T} to the next section. First of all, an algebraic equation for conservation of volume can be derived that relates the thickness of various layers within the fiber and balances with any melt-water exiting into the vessel (U). After exploiting the circular symmetry in the fiber, this volume constraint is differentiated in time to obtain

$$\partial_t s_g = -\frac{(\rho_w - \rho_i)s_{iw}\partial_t s_{iw}}{\rho_i s_g} + \frac{\rho_w \partial_t U}{2\pi L^f \rho_i s_g}, \quad (1)$$

where ρ_w and ρ_i are the water and ice densities respectively. Note that this equation is an ordinary differential equation (ODE) for the variable $s_g(t)$. A similar volume conservation equation governs the vessel gas bubble radius $r(t)$

$$\partial_t r = -\frac{N\partial_t U + \partial_t U_r}{2\pi L^v r}, \quad (2)$$

which involves an additional term arising from root water U drawn into the xylem vessel network. Note that the $\partial_t U$ term is multiplied here by N , which is the average number of fibers connected to each vessel. The dynamics of the ice-water interface s_{iw} is governed by a phase change process that obeys the Stefan condition

$$\partial_t s_{iw} = -\frac{k_w/\rho_w}{E_w - E_i} \partial_n \mathcal{T} + \frac{\partial_t U}{2\pi L^f s_{iw}}, \quad (3)$$

where k_w is the thermal conductivity of water, $(E_w - E_i)$ is the latent heat, and $\partial_n \mathcal{T} \equiv \nabla_y \mathcal{T} \cdot \vec{n}$ denotes the normal heat flux.

The two remaining equations are obtained by applying Darcy's law for flow in porous media. The liquid flux through the porous fiber-vessel wall obeys

$$\partial_t U = -\frac{\mathcal{L}\mathcal{A}_{fv}}{N} \left(p_w^v - p_w^f - C_s \mathcal{R}\mathcal{T}(R^v, t) + p_{ice} \right) \quad (4)$$

where $\mathcal{A}_{fv} = 2\pi R^v L^v$ is the surface area of the fiber-vessel wall and \mathcal{L} is its hydraulic conductivity. The term in parentheses represents a balance at the fiber-vessel wall between four pressures: vessel and fiber liquid pressures, $p_w^v(t)$ and $p_w^f(t)$; osmotic pressure deriving from the sap sugar concentration C_s ; and cryostatic suction p_{ice} which is an ice-water surface tension that is zero under thawing conditions, but nonzero when the fiber is completely frozen and the adjacent vessel contains liquid sap. A second application of Darcy's gives the volume flux of root water as

$$\partial_t U_r = -\mathcal{C}_r \mathcal{L}_r \mathcal{A}_r (p_w^v - p_{soil}), \quad (5)$$

where \mathcal{L}_r is the root hydraulic conductivity, \mathcal{A}_r is the root area (per vessel), and p_{soil} is the soil water pressure. According to Henzler et al. (1999), the roots function as a partial check valve in the sense that aquaporin membranes controlling root water transport are more permeable to inflow than to outflow. This effect is incorporated through a reflection coefficient $\mathcal{C}_r \in [0, 1]$ that takes the value $\mathcal{C}_r = \mathcal{C}_{r,in} = 1$ for inflow (when $p_w^v \leq p_{soil}$) and $\mathcal{C}_r = \mathcal{C}_{r,out} \in [0, 1)$ for outflow (when

$p_w^v > p_{soil}$). The lower limit $\mathcal{C}_{r,out} = 0$ corresponds to the case of no root outflow (which was assumed by Graf et al. (2015)) whereas the upper limit $\mathcal{C}_{r,out} = 1$ represents the symmetric case where root inflow and outflow experience equal resistance. We propose using an intermediate value of $\mathcal{C}_{r,out} = 0.2$, which is consistent with experiments of Henzler et al. (1999) on legumes, and of Steudle and Peterson (1998) on woody plants (although a values as large as $\mathcal{C}_{r,out} = 0.7$ have been suggested by Tyree et al. (1994)).

The only quantities in the above equations that remain to be specified are the vessel and fiber liquid pressures p_w^v and p_w^f . In the vessel, the sap pressure satisfies

$$p_g^v(t) = \frac{\rho_g^v(t)\mathcal{R}T_c}{M_g} - \frac{2\sigma_{gw}}{r(t)}, \quad (6)$$

which represents a balance between gas pressure (from the ideal gas law) and surface tension at the gas bubble interface (from the Young-Laplace equation). Here, $\rho_g^v(t)$ is the vessel gas density and σ_{gw} is the gas-liquid surface tension. The gas density is related to the volumes $V_w^v(t)$ and $V_g^v(t)$ of the vessel sap and gas regions by

$$\rho_g^v(t) = \left(\frac{V_g^v(0) + \mathcal{H}V_w^v(0)}{V_g^v(t) + \mathcal{H}V_w^v(t)} \right) \rho_g^v(0), \quad (7)$$

which accounts for gas dissolving in the sap via terms involving Henry's constant \mathcal{H} . Finally, the cell volume quantities are determined by simple geometric constraints

$$V_g^v(t) = \pi L^v r(t)^2 \quad \text{and} \quad V_w^v(t) = \pi L^v ((R^v)^2 - r(t)^2). \quad (8)$$

An analogous set of equations govern the fiber water pressure $p_w^f(t)$ but are not included here.

Recall that the ODEs (1)–(5) along with the algebraic constraints (6)–(8) describe the dynamics within the fiber and vessel during a thawing phase only, when a fiber in the midst of thawing lies adjacent to a vessel that is completely thawed. There are five additional cases corresponding to the various freeze–thaw states within the fiber and vessel, and each case leads to a modification of the governing equations detailed in Graf et al. (2015).

3.3. Homogenized two-scale model for heat transport

To complete the model description we must derive two additional equations describing heat transport: the first capturing microscale effects that arise from phase change within the fibers and vessels; and the second governing macroscale effects throughout the xylem that are driven by ambient temperature variations. However, the temperatures on the two scales are tightly coupled and so that extra care must be taken to properly account for the transfer of heat energy between the micro- and macro-scales. For this purpose, we apply the method of periodic homogenization or two-scale convergence (Allaire, 1992) which posits that in a material such as sapwood having a clear separation of scales, the detailed microscale dynamics can be represented by a simpler problem defined on a reference cell \mathcal{Y} . For reasons of simplicity, \mathcal{Y} is typically assumed to have radial symmetry, which is not the case for the microscale geometry in Figure 2c; nevertheless, we can still define a modified reference cell that has the requisite symmetry. Because the essential freeze–thaw processes that govern pressure generation occur within fibers, we choose a fiber-centric coordinate system with radial variable y , in which the fiber is placed in the middle of a square reference cell having side length ε (see Figure 4a). Since the vessel is so much larger than the fiber,

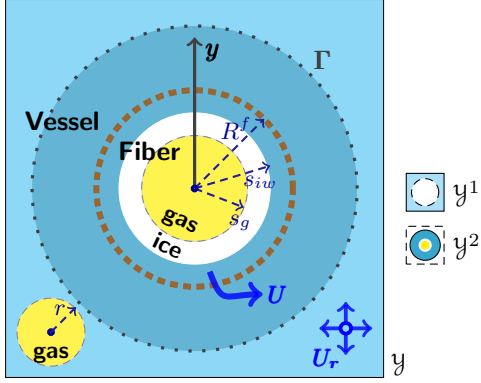
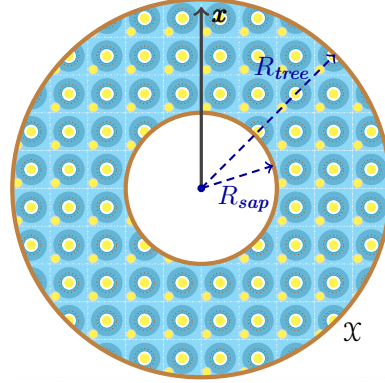
(a) Reference cell, $\mathcal{Y} = \mathcal{Y}^1 \cup \Gamma \cup \mathcal{Y}^2$.(b) Stem cross-section \mathcal{X} tiled with reference cells.

Figure 4: (a) The reference cell \mathcal{Y} containing a fiber located at the center (the brown dashed line is the fiber wall) outside of which lies the vessel. For the purposes of the periodic homogenization process, an artificial boundary Γ (outer dotted circle) is introduced that separates \mathcal{Y} into two sub-regions: \mathcal{Y}^2 , a fiber–vessel overlap region where heat diffusion is slow (shaded in medium blue); and \mathcal{Y}^1 , the outer portion of the vessel region where diffusion is relatively fast (light blue). A gas bubble of radius r is depicted in the lower-left corner, and the root water source U_r in the lower-right. (b) An annular sapwood cross-section is tiled periodically with copies of the reference cell from (a). Mature trees contains a non-conducting heartwood region extending out to radius $x = R_{sap}$, whereas younger saplings may have no heartwood ($R_{sap} = 0$).

it appears simply as a sap reservoir from the fiber perspective. Consequently, we consider the vessel as the region of the reference cell lying outside the fiber, as depicted in Figure 4a (which in some sense “turns the vessel inside-out”). In order that this modified reference cell remains consistent with the original fiber–vessel geometry in Figure 2c, we impose a simple volume constraint

$$\pi(R^v)^2 + \pi(R^f)^2 N = \varepsilon^2, \quad (9)$$

which ensures that each reference cell captures the net influence of one vessel and N adjacent fibers. Although Figure 4a depicts the vessel gas as a circular region in the lower-left corner, the gas is not strictly assigned to any physical location otherwise the radial symmetry would be broken. Instead, it is represented in terms of the radius r of the equivalent gas bubble along with the fraction of gas in dissolved form. As a result, the equations from the previous section remain identical despite this apparent change in reference cell geometry.

Next we exploit the regular, quasi-periodic microstructure of sapwood and view the stem as being constructed of a periodic array of reference cells as pictured in Figure 4b. The macroscopic domain \mathcal{X} is the 2D cross-section of an annular cylinder having outer radius $x = R_{tree}$ and inner radius $x = R_{sap}$ bounding the non-conductive heartwood. Our aim is now to derive two equations for heat transport: one on the reference cell that incorporates local variations in temperature due to freeze–thaw processes occurring in a given reference cell at location $x \in \mathcal{X}$; and a second equation capturing macroscopic heat transport throughout \mathcal{X} in response to ambient temperature fluctuations, combined with the local effects. The main objective of the periodic homogenization process is to derive appropriate heat transport coefficients for the macroscale heat equation that incorporate the effects of the microscale by averaging the solution of the reference cell problem \mathcal{Y} appropriately. We also note that the reference cell size ε plays a dual role in homogenization: it can be considered as a physical dimension but must also be viewed asymptotically in the limit as

$\varepsilon \rightarrow 0$ to obtain the averaged effect of the microscale freeze–thaw process on the macroscale.

We now summarize the essential aspects of the periodic homogenization procedure, for which complete mathematical details are provided in Konrad et al. (2017). For technical reasons, the reference cell \mathcal{Y} is separated into two sub-regions (\mathcal{Y}^2 and \mathcal{Y}^1) pictured in Figure 4a, where \mathcal{Y}^2 refers to the fiber plus the inner portion of the vessel where heat diffuses slowly, whereas \mathcal{Y}^1 is the remaining outer portion of the vessel where diffusion is fast compared to \mathcal{Y}^2 . The curve Γ is an artificial boundary separating \mathcal{Y}^1 from \mathcal{Y}^2 so that $\mathcal{Y}(x, t) = \mathcal{Y}^1 \cup \Gamma \cup \mathcal{Y}^2(x, t)$. Note that an implicit time and space dependence appears in \mathcal{Y}^2 (and hence also \mathcal{Y}) owing to the motion of phase boundaries that alters the geometry of \mathcal{Y} depending on the specific location x (although our notation will often omit this dependence). Our aim is then to derive two heat diffusion equations, one for $\mathcal{T}(x, y, t)$ on the microscale domain $\mathcal{Y}^2 \times \mathcal{X}$ and the other for $T(y, t)$ on the macroscale domain \mathcal{X} .

The governing equations are stated in a mixed temperature–enthalpy formulation in order to properly capture phase transitions. To this end we define $T(x, t)$ and $E(x, t)$ as the macroscale temperature and enthalpy variables, which are both constant inside \mathcal{Y}^1 and thus depend only on the macroscale spatial coordinate x . The corresponding microscale variables on $\mathcal{Y}^2(x, t)$ are $\mathcal{T}(x, y, t)$ and $\mathcal{E}(x, y, t)$, which vary at each point in the macroscopic domain as well as the microscale y . We impose the usual temperature–enthalpy relationship on both $T = \omega(E)$ and $\mathcal{T} = \omega(\mathcal{E})$ where

$$\omega(E) = \begin{cases} \frac{E}{c_i}, & \text{if } E < E_i - \delta_i, \\ T_c - \frac{2E - E_i - E_w}{2c_\infty}, & \text{if } E_i - \delta_i \leq E \leq E_w + \delta_w, \\ T_c + \frac{E - E_w}{c_w}, & \text{if } E_w + \delta_w < E, \end{cases} \quad (10)$$

captures the change in phase that occurs at the critical (melting) temperature T_c . This is a piecewise function consisting of two linear segments with slopes c_i^{-1} in ice and c_w^{-1} in liquid, connected by a steep layer with slope c_∞^{-1} (where $c_\infty \approx 10^7$). Here $c_{w,i}$ refers to the specific heat capacities of water and ice, while $\delta_i = \frac{c_i(E_w - E_i)}{2(c_\infty - c_i)}$ and $\delta_w = \frac{c_w(E_w - E_i)}{2(c_\infty - c_w)}$ are chosen to ensure $\omega(E)$ is continuous.

Heat transport within the liquid-filled subregion \mathcal{Y}^2 is governed by the usual heat equation

$$c_w \partial_t \mathcal{T} - \partial_y \left(D(\mathcal{E}) \partial_y \mathcal{T} \right) = 0 \quad \text{in } \mathcal{Y}^2(x, t) \times \mathcal{X}, \quad (11)$$

where D is a thermal diffusion coefficient that is also a piecewise linear function of enthalpy (Visintin, 1996):

$$D(\mathcal{E}) = \begin{cases} \frac{k_i}{\rho_i}, & \text{if } \mathcal{E} < E_i, \\ \frac{k_i}{\rho_i} + \frac{\mathcal{E} - E_i}{E_w - E_i} \left(\frac{k_w}{\rho_w} - \frac{k_i}{\rho_i} \right), & \text{if } E_i \leq \mathcal{E} \leq E_w, \\ \frac{k_w}{\rho_w}, & \text{if } E_w < \mathcal{E}. \end{cases} \quad (12)$$

The partial differential equation (11) requires boundary conditions on the inner ($\partial\mathcal{Y}^2$) and outer (Γ) boundaries of \mathcal{Y}^2 , which are

$$\mathcal{T} = T_c \quad \text{on } \partial\mathcal{Y}^2(x, t) \times \mathcal{X} \quad (\text{phase-change boundary}), \quad (13)$$

$$\mathcal{T} = T \quad \text{on } \Gamma \times \mathcal{X} \quad (\text{coupling to macro-temperature}). \quad (14)$$

The homogenization procedure that we apply next to obtain a macroscale heat equation is more complicated and requires first taking $y = x/\varepsilon$ in the microscale problem and then expanding the

solution asymptotically as $\varepsilon \rightarrow 0$, which is referred to as the *two-scale limiting process*. The governing equation is written in an integral (weak) formulation, but after approximating the resulting integral terms in the $\varepsilon \rightarrow 0$ limit one obtains the following strong formulation of the limit problem:

$$\partial_t E - \partial_x \left(\Pi D(E) \partial_x T \right) = \frac{1}{|\mathcal{Y}^1|} \int_{\Gamma} D(\varepsilon) \partial_n \mathcal{T} dS \quad \text{in } \mathcal{X}. \quad (15)$$

Note that this is an alternate form of the heat diffusion equation, written in a mixed temperature–enthalpy form that implicitly captures parameter discontinuities across phase interfaces. There are two new terms appearing in Eq. (15) via the homogenization process that are critically important in properly capturing the influence of the microscale problems on the macroscale:

- The homogenized diffusion operator contains an extra constant factor Π , which is a purely geometric quantity consisting of a 2×2 matrix with entries

$$\Pi_{ij} = \frac{1}{|\mathcal{Y}^1|} \int_{\mathcal{Y}^1} (\delta_{ij} + \partial_y \mu_i) dy. \quad (16)$$

Here, δ_{ij} is the Kronecker delta symbol and $\mu_i(y)$ are solutions to simple elliptic PDE problems on the reference cell \mathcal{Y}^1 (Allaire, 1992).

- The source term on the right hand side is a surface integral over the artificial boundary Γ of the microscopic heat flux.

It is important to recognize here that the temperature–enthalpy relationship $T = \omega(E)$ in (10) involves the critical temperature, T_c . Within the fiber (which contains pure water) we take $T_c = 0^\circ\text{C}$, but in the macroscale problem T_c must be replaced with

$$T_{c,sap} = T_c - \frac{K_b C_s}{\rho_w}, \quad (17)$$

where $K_b = 1.853$ is the cryoscopic (or Blagden’s) constant. This accounts for the freezing point depression or FPD that arises due to dissolved solutes (primarily sugar) in the vessel sap. Finally, the PDE (15) is supplemented with the boundary condition

$$T = T_a(t) \quad \text{on } \partial\mathcal{X}, \quad (18)$$

which sets the outer stem surface temperature equal to a given ambient air temperature and is what ultimately drives the freeze–thaw process. Complete details of the homogenization procedure can be found in Konrad et al. (2017), and we also refer the interested reader to the work of Chavarría-Krauser and Ptashnyk (2013) who applied periodic homogenization to a related problem involving osmotic transport in non-woody plants.

The parameter values appearing in these equations are taken mostly from previous work (Graf et al., 2015; Konrad et al., 2017) that focused on comparisons to experimental data from black walnut. These parameters are summarized in Table 1, with a few small adjustments for red/sugar maple as indicated. The “base case” that is indicated there corresponds to a sugar maple sapling with diameter of 14 cm that has sap sugar content of 3% by mass.

Table 1: Model parameters used in the base case simulations are taken from Graf et al. (2015), unless otherwise indicated. Modifications to parameters R_{tree} , R_{sap} , γ_s for comparison with the red/sugar maple experiments are detailed in the text.

Symbol	Description	Values	Units
<i>Variables (functions of time t and space x or y):</i>			
s_{iw}, s_g	fiber interface locations		m
r	vessel bubble radius		m
U	water transferred from fiber to vessel		m^3
U_r	root water uptake		m^3
\mathcal{T}, T	temperature		$^\circ\text{C}$
p	pressure		Pa
ρ	density		kg m^{-3}
V	volume		m^3
<i>(Subscripts: i, w, g for ice, water/sap, gas; Superscripts: f, v for fiber, vessel)</i>			
<i>Tree physiological parameters:</i>			
\mathcal{A}_{fv}	surface area of fiber–vessel wall	6.28×10^{-8}	m^2
\mathcal{A}_r	root area per vessel = $\mathcal{A}_{tree}(R^v/R_{tree})^2$	1.14×10^{-6}	m^2
\mathcal{C}_r	root reflection coefficient, Eq. (5)	0.2(out), 1.0(in)	–
ε	side length of reference cell, Eq. (9)	4.33×10^{-5}	m
L^f	length of fiber	1.0×10^{-3}	m
L^v	length of vessel element	5.0×10^{-4}	m
\mathcal{L}	conductivity of fiber–vessel wall	5.54×10^{-13}	$\text{m s}^{-1} \text{Pa}^{-1}$
\mathcal{L}_r	root conductivity	2.7×10^{-16}	$\text{m s}^{-1} \text{Pa}^{-1}$
N	number of fibers per vessel	16	–
R^f	inside radius of fiber	3.5×10^{-6}	m
R^v	inside radius of vessel	2.0×10^{-5}	m
<i>Physical constants:</i>			
\mathcal{H}	Henry’s constant for air dissolved in water	0.0274	–
K_b	cryoscopic (Blagden) constant	1.853	$\text{kg } ^\circ\text{C mol}^{-1}$
M_g	molar mass of gas (air)	0.029	kg mol^{-1}
M_s	molar mass of sugar (sucrose)	0.3423	kg mol^{-1}
\mathcal{R}	universal gas constant	8.314	$\text{J } ^\circ\text{C}^{-1} \text{mol}^{-1}$
<i>Water phase properties:</i>			
c_i, c_w	specific heat capacity	2100 4180	$\text{J } ^\circ\text{C}^{-1} \text{kg}^{-1}$
E_i, E_w	enthalpy at T_c	574 907	kJ kg^{-1}
k_i, k_w	thermal conductivity	2.22 0.556	$\text{W m}^{-1} ^\circ\text{C}^{-1}$
ρ_i, ρ_w	density	917 1000	kg m^{-3}
σ_{iw}, σ_{gw}	surface tension (Fowler and Krantz, 1994)	0.033 0.076	N m^{-1}
c_∞	enthalpy regularization parameter, Eq. (10)	1.0×10^7	$\text{J } ^\circ\text{C}^{-1} \text{kg}^{-1}$
<i>Base case parameters:</i>			
R_{tree}	tree stem radius	0.07	m
R_{sap}	sapwood/heartwood boundary	0	m
θ	heartwood fraction = R_{sap}/R_{tree}	0	–
γ_s	sap sugar content (mass fraction)	0.03	–
C_s	sap sugar concentration = $\gamma_s \rho_w / M_s$	87.6	mol m^{-3}
$T_{c,sap}$	freezing point depression (FPD) = $-K_b C_s / \rho_w$	-0.162	$^\circ\text{C}$
p_{soil}	soil pressure at roots = $p_w^v(0)$	2.03×10^5	Pa

3.4. Numerical solution algorithm

The exudation model equations consist of five ODEs (1)–(5) for the microscale variables along with two PDEs (11) and (15) for temperature. We apply the method-of-lines to discretize the temperature equations by first approximating all spatial derivatives using a finite volume approach, which yields a large coupled system of time-dependent ODEs. The macroscale variable x is discretized at n_x equally-spaced points, with n_x chosen between 25–50 (depending on tree size) so that the grid spacing $\Delta x = (R_{tree} - R_{sap})/n_x$ is less than 0.3 cm, which we find is sufficient in practice to resolve the freezing and thawing fronts. For the microscale problem, we obtain satisfactory accuracy with a relatively coarse grid having $n_y = 6$ points.

Assembling the semi-discrete equations for temperature together with the remaining ODEs and algebraic constraints within each reference cell at location x yields a coupled differential–algebraic system that is integrated in time using the stiff solver `ode15s` in MATLAB (2020). We note that a stiff solver is required for this problem because of the widely disparate time scales arising from the disparate dynamics on the cellular level and within the tree stem. The strong coupling between micro- and macroscale temperatures is handled by applying a split-step time discretization: first, the microscale equations for $s_g, s_{iw}, r, U, U_r, \mathcal{T}$ in the reference cell at each discrete point are advanced in time while holding the macroscale temperature T constant; following that, T is advanced in time by holding other variables constant. More details related to implementation of the multiscale algorithm can be found in Graf et al. (2015).

4. Results

4.1. Experimental data and temperature smoothing

Based on the experiments described in Section 2, we have chosen to focus our attention on two red maple trees (which we label R1 and R2 for convenience) and one sugar maple (labelled S1). A more detailed description of these experiments that emphasizes the temperature measurements can be found in Wilmot (2006). Air temperature data for all three trees are displayed in Figure 5(left) over periods of 33 days (R1,R2) and 45 days (S1). These samples were singled out for comparison with numerical simulations because the air temperature in each case features several pronounced freeze–thaw cycles during the measurement period. Note that the temperature plot for sugar maple in Figure 5b-i includes a second curve (red, dashed) showing the soil temperature at 30 cm depth which for most of the 45-day period remains positive, even during times when the air temperature is below zero. This provides strong evidence in support of the earlier assumption A10 that liquid water is available for root uptake even under freezing conditions.

Although these air temperature measurements have an inherent large-scale oscillation that varies roughly on a daily period, the two zoomed-in views in Figures 5a,b-i show that there are also significant fluctuations from one 15-minute time interval to the next. These rapid changes are likely due to a combination of local temperature variability and measurement errors and are a major distinguishing feature that sets these field measurements apart from others obtained under carefully-controlled laboratory conditions. Indeed, just such an experiment on black walnut trees (Améglío et al., 2001) was used to validate a previous incarnation of our multiscale model (Graf et al., 2015) where the input temperatures was specified as a given smoothly-varying function of time. Consequently, our measurements for red/sugar maple provide an excellent opportunity to validate the model under more realistic conditions.

Because our exudation model is based on differential equations that expect the ambient temperature $T_a(t)$ in Eq. (18) to vary continuously in time, we need to impose some regularization to

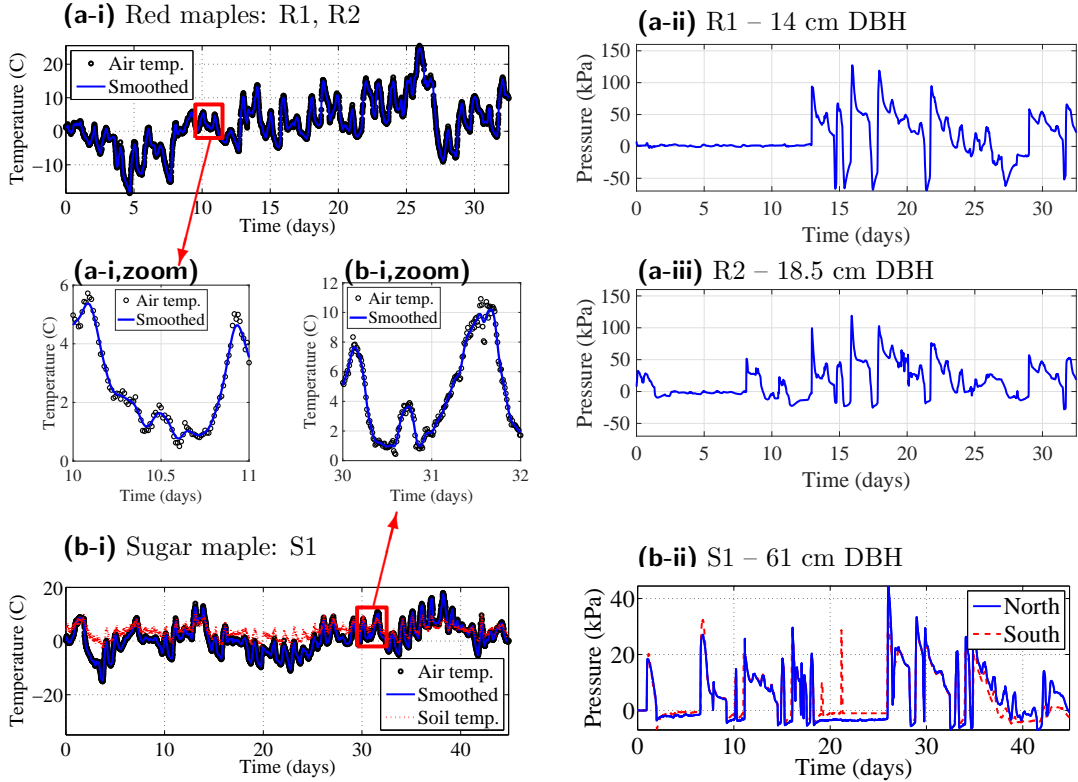


Figure 5: (Left, a-i and b-i) Measured air temperatures are plotted for two red maple trees (R1, R2) and one sugar maple (S1) from the UVM experiments. The temperature plot for sugar maple in (b-i) also includes values of soil temperature (at 30 cm depth) which remain mostly above 0°C , hence supporting the assumption that liquid water is present even when air temperatures are below freezing. The raw temperature data (blue points) are regularized by applying a simple weighted-average smoothing – the resulting smoothed data are shown alongside the original temperatures in the zoomed views (a-i,zoom, b-i,zoom). (Right, a-ii, a-iii and b-ii) Corresponding pressure data for the three trees. An extra set of pressure measurements is included in the sugar maple plot (b-ii) to illustrate the impact of taking measurements on the north/south sides of the stem.

smooth the raw temperature data. To this end, we apply a simple weighted-average smoothing procedure in which each temperature value is averaged with its two neighbouring points using weights $[\frac{1}{4}, \frac{1}{2}, \frac{1}{4}]$, with this procedure being repeated 10 times. The smoothed temperature is displayed as a solid curve along with the raw data in the two zoomed plots in Figures 5a,b-i, from which it is clear that this procedure eliminates many irregularities without sacrificing much detail. There is of course a risk that genuine fine-scale variations in temperature are suppressed, but we have observed that reducing the number of smoothing steps has no appreciable effect on the model simulations. This is consistent with the results in Section 4.3 which show that exudation behavior is dominated by the location of temperature zero-crossings and influenced much less by variations in $T_a(t)$ away from zero.

4.2. Parameter sensitivity study

To study the relative importance of various geometric and physical properties on the sap exudation process, we identify a base case using the parameters listed in Table 1 and then vary certain parameters relative to these base values. Our chosen base case represents a young sapling with

$R_{tree} = 0.07$ m and $R_{sap} = 0$ that hasn't yet developed any heartwood, and we use our best estimates for the remaining parameters. To mimic a repeated sequence of diurnal freeze–thaw events, we impose a simple sinusoidally-varying ambient temperature, $T_a(t) = 5 - 15 \sin(2\pi t/86400)$, that oscillates between -10 and $+20^\circ\text{C}$ over a time interval of 5 days. This is admittedly a fairly extreme range of temperatures, but it does ensure that the entire stem is able to freeze and thaw completely during each cycle. Results of the parameter sensitivity study are presented in Figure 6 as plots of root water uptake U_r and averaged pressure $\bar{p} = \frac{1}{|\mathcal{A}|} \int_{\mathcal{A}} p_w^v dA$, where $|\mathcal{A}|$ is the area of the annular-shaped sapwood region. This averaged pressure is a better approximation than any specific point value for what is measured by a pressure gauge inserted into a taphole.

The results plotted in Figure 6 focus on variations in five key model parameters and how they affect the behaviour of pressure and root uptake:

- (a) Tree radius (R_{tree}), which is the primary geometric parameter that distinguishes between the mature trees in this study and younger saplings. Values of R_{tree} are selected between 5–30 cm which covers the range of tree sizes in the experiment discussed in Section 2 and the corresponding \bar{p} and U_r solution curves are shown in Figure 6a. Note that the curve corresponding to the base case ($R_{tree} = 0.07$) is always drawn as a solid blue line and is highlighted in the legend with a “*”.
- (b) Heartwood fraction ($\theta = R_{sap}/R_{tree}$), which is zero for young saplings but can be significantly larger in mature trees. The red/sugar maples considered in this study are from a well-established area of the forest in which trees typically have 25–50% of their basal area taken up by heartwood (with lower fractions in smaller trees and higher fractions in larger trees). Most of these trees have been tapped annually for maple collection over a period of 50–60 years, which generates a column of non-conductive wood that extend above and below each year's taphole (typically by a distance of ± 0.25 m). Therefore while there is undoubtedly some heartwood in these trees, there is also considerable non-conductive wood within the tapping band as a result of tapping history. We therefore chose values of heartwood fraction within the range $\theta \in [0, 0.7]$, which is consistent with the measurements of Duchesne et al. (2016) who found a maximum value of $\theta \approx 0.45$, while also allowing for even higher values such as those reported by Baral et al. (2017).
- (c) Total root area ($\mathcal{A}_{tree} = \mathcal{A}_r(R_{tree}/R^v)^2$), which is related to the root area per vessel (\mathcal{A}_r) by scaling proportionally to cross-sectional area. Because values of \mathcal{A}_{tree} for red maple have been reported to lie in the range 10.4 to 18.6 m² (Day and Harris, 2007), we choose a value of $\mathcal{A}_{tree} = 14$ for the base case that lies near the middle of this range; scaling by the area ratio yields a corresponding root area per vessel of $\mathcal{A}_r = \mathcal{A}_{tree}(R^v/R_{tree})^2 \approx 1.14 \times 10^{-6}$ m². For the sensitivity results shown in Figure 6c, we have actually selected a wider range of $\mathcal{A}_{tree} \in [1, 100]$.
- (d) Root reflection coefficient for outflow ($\mathcal{C}_{r,out}$), which is the major extension we have made to the original exudation model that assumed $\mathcal{C}_{r,out} \equiv 0$ (Graf et al., 2015). There is an extensive literature suggesting that root conductivity in a wide range of trees and plants is not constant but rather exhibits both seasonal and diurnal variations controlled by aquaporin membranes within the roots (Javot and Maurel, 2002; Steudle, 1994). Furthermore many root systems exhibit an asymmetry in conductivity between inflow and outflow, which can be modelled by means of a reflection coefficient $\mathcal{C}_{r,out}$ (Knipfer and Fricke, 2010; Steudle, 1994)

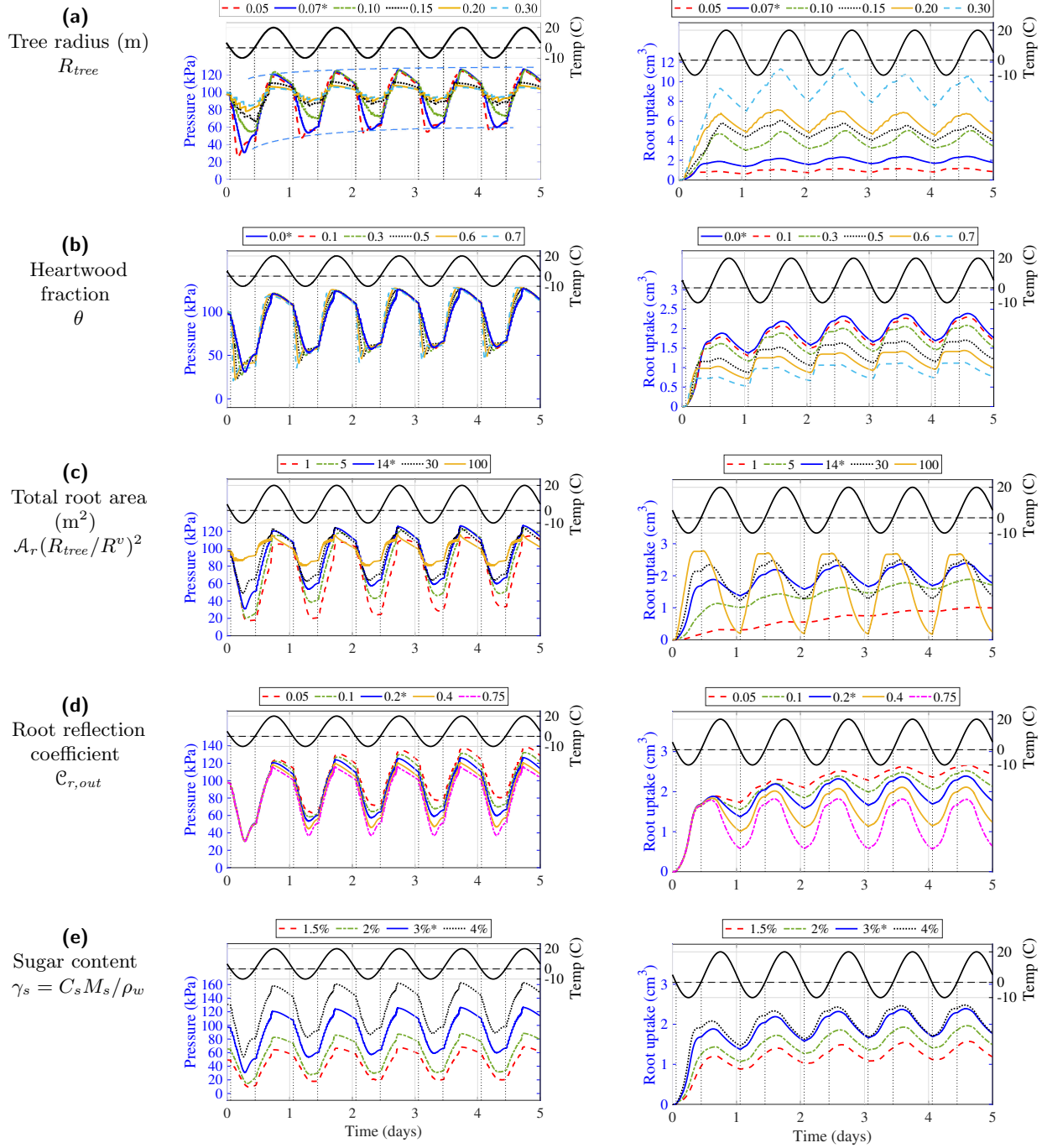


Figure 6: Parameter sensitivity study showing the effects on stem-averaged pressure (\bar{p}) and root water uptake (U_r) due to variations in five parameters: (a) tree radius, (b) heartwood fraction, (c) total root area, (d) root reflection coefficient, and (e) sap sugar content. In each plot, the parameter value from the base case is highlighted in the legend with a “*” and the corresponding curve is drawn with a blue solid line. The dotted vertical lines indicate freeze and thaw events, when the ambient temperature crosses zero. The “envelope curves” tracing max-min points for the R_{tree} base-case pressure are shown as two dashed blue lines (a, left).

that is less than 1 and can drop to $\mathcal{C}_{r,out} = 0.2$ or less (Henzler et al., 1999). Among the few studies we are aware of that mention maple trees, O’Leary (1965) observed no appreciable root outflux ($\mathcal{C}_{r,out} \approx 0$) whereas Dawson (1993) observed more moderate asymmetry (with $\mathcal{C}_{r,out}$ significantly greater than 0). In the absence of any reliable estimates specific to maple, we assume a base value of $\mathcal{C}_{r,out} = 0.2$ that is constant in time, and compare with other values from the range $[0.05, 0.75]$ in Figure 6d.

- (e) Sap sugar content by mass (γ_s), which is related to sugar concentration by $\gamma_s = C_s M_s / \rho_w$, where M_s the molar mass of sugar. High sugar content is an important feature distinguishing maples from other species that exude sap. Sugar maple sap contains roughly 3% sugar on average during the sap harvest season (Larochelle et al., 1998) but can be as high as 5% in some trees (Jones and Alli, 1987). On the other hand, red maples tend to have a lower sugar content that is closer to 2% on average. Sugar content also varies significantly between seasons, between trees, and also throughout a given season (starting a bit low, rising for the first 1/4 to 1/3 of the season, then steadily dropping towards the end). We have therefore chosen a representative value of 3% ($\gamma_s = 0.03$) for the base case along with several other values selected from the range 1.5 to 4.0% as depicted in Figure 6e.

This parameter sensitivity study is partly based on results from Zarrinderakht (2017), which includes additional results not reported here.

4.3. Numerical simulations of red and sugar maple

We next apply the MATLAB code to simulate the three trees singled out in Section 4.1, taking the smoothed temperature curves depicted in Figures 5a,b-i as input for the ambient temperature $T_a(t)$. Two simulations are performed for red maple trees (R1,R2) with stem radii $R_{tree} = 7$ and 9.25 cm, both consisting entirely of sapwood ($R_{sap} = 0$) since they are relatively young trees. The sugar content for these trees is set to 1.8% which is a representative value for mid-to-late season, but otherwise all model parameters are the same as the base case in Table 1. The equations were integrated over a period of 27 days, which covers the majority of the freeze–thaw events occurring in the air temperature measurements. The resulting plots of simulated average pressure \bar{p} are displayed in Figures 7a,b alongside the corresponding experimental measurements. The smoothed temperature data are shown at the top of each plot, with dotted vertical lines drawn at each time when $T_a(t)$ crosses 0°C for easy identification of freeze and thaw events.

One sugar maple simulation (S1) is performed with ambient temperature $T_a(t)$ taken equal to the smoothed temperature from Figure 5b-i and stem radius set to $R_{tree} = 30.5$ cm. Because this is a more mature tree than the red maples, we assume that the heartwood extends half-way through the stem and take $\theta = \frac{1}{2}$. The resulting pressure curves are displayed in Figure 7c, with the experimental pressure taken from the north-side sensor measurements (refer to Figure 5b-ii).

5. Discussion

5.1. Thaw events trigger pressure spikes

Based on the experimental measurements of pressure in the right-hand plots of Figure 5(right), an characteristic feature of all three trees is the spikes or rapid increases in pressure that occur at certain discrete times. By viewing these plots alongside the corresponding temperature curves from Figure 5(left) we observe that the spikes coincide with the times that thaw events occur, which is

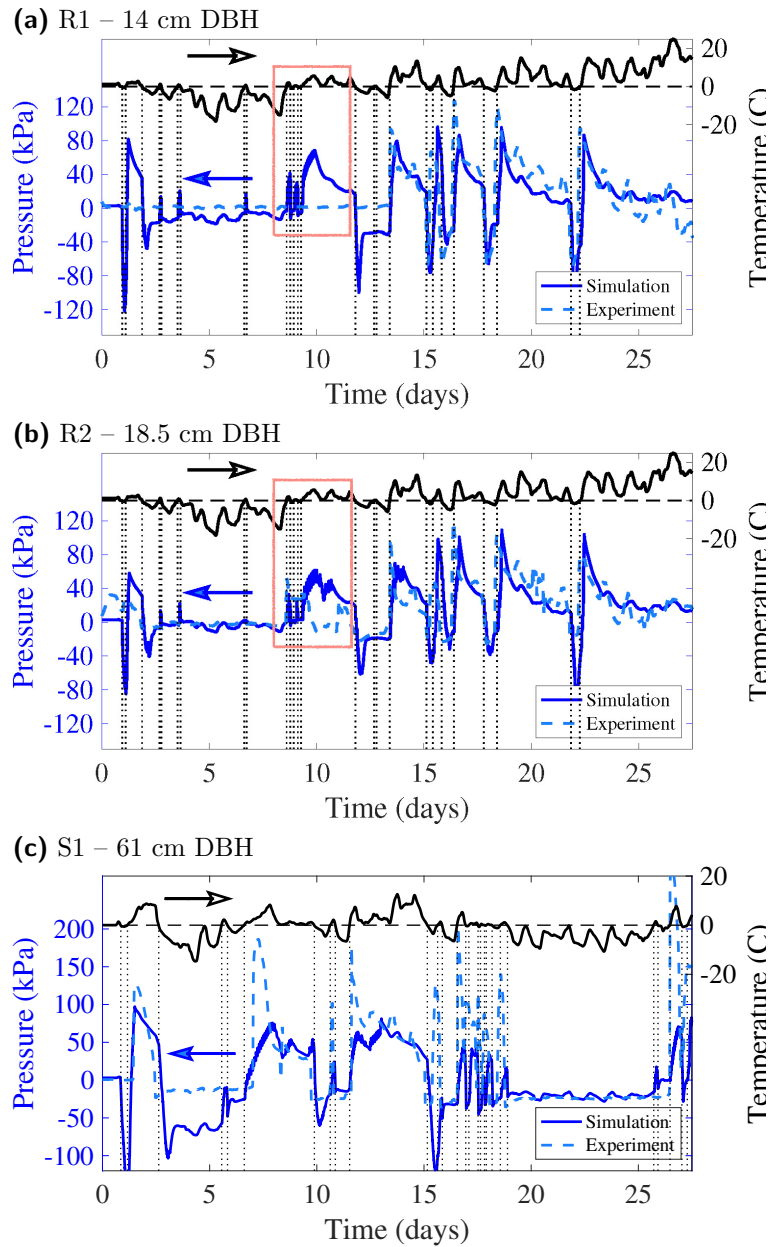


Figure 7: Comparison of stem pressure from experiments (solid blue lines) and simulations (dashed cyan lines) for red maple (a,b) and sugar maple trees (c). The smoothed temperature data are also displayed on the top set of axes, and each freeze–thaw event is highlighted with a vertical dotted line (at each time where temperature crosses 0°C) so that these events are easily connected with corresponding pressure spikes. A “weak thaw” event is highlighted with a pink box in the R1,R2 simulations (a,b).

when the temperature increases past the melting point (this correspondence is much more clearly seen in the plots appearing later in Figure 7). After thawing and for as long as the temperature remains above zero, each such spike is followed by a time period of gradually falling pressure, where the rate of decrease appears fairly consistent between thawing events. This behavior is consistent with other experimental pressure measurements in maple and related species (Tyree, 1983; Cortes and Sinclair, 1985; Améglio et al., 2001; Ewers et al., 2001). The timing, amplitude and decay of these pressure spikes will form the main points of comparison when we study the numerical simulations in Section 5.3.

It is also worth noting that for the sugar maple only, two pressure curves are provided (see Figure 5b-ii) that correspond to measurements taken from two sensors placed opposite each other on the north and south sides of the stem. The measured pressure variations are qualitatively very similar, especially when one focuses on the timing and height of the pressure spikes and their subsequent decay. A notable exception is the two spikes recorded by the south sensor around day 20 that do not have matching spikes in the north side data. Because these two spikes correspond to especially short thaw events (in which temperature exceeds zero for only a brief time interval) it is likely that they are not experienced as thawing events throughout the entire tree. For this reason, we have chosen to use the north-side pressure data for comparison with the S1 simulation.

5.2. Exudation is most sensitive to R_{tree} and γ_s

The parameter sensitivity study in Figure 6 will allow us to identify suitable values to use for parameters in the experimental comparisons in the next section, as well as pinpointing those parameters that have the greatest impact on the model solution and hence are most important to estimate accurately. We begin by comparing the qualitative features of the solutions in Figure 6a for different tree radius, R_{tree} . In all cases we observe that average stem pressure \bar{p} behaves similar to the experiments in that it exhibits a steep increase whenever temperature increases past the freezing point. This is followed by a gradual decline while the temperature remains positive but as soon as temperature falls below zero there is a similarly steep drop in pressure, after which the cycle repeats. The amplitude of the pressure oscillations decreases for larger radius trees, which is consistent with there being a larger sapwood area to freeze and hence a correspondingly larger water uptake. What is perhaps more important for exudation is the “envelope curves” that trace out max/min points of the pressure (see blue dashed curves in Figure 6a, left) which exhibit an upward trend that reflects a build-up in exudation pressure over time. The pressure envelope is affected significantly by changes in R_{tree} in that the amplitude of the pressure oscillations decreases with increased R_{tree} ; however the time-averaged pressure (which sits midway between the envelope curves) is relatively insensitive to changes in radius. This contrasts with the relatively huge increase in root water uptake for higher values of R_{tree} , but again these larger trees have a proportionally greater volume to freeze and over which to distribute the stored pressure.

The simulations in Figure 6b correspond to values of heartwood fraction θ between 0 and 0.7. Clearly, both the shape of the pressure oscillations and the exudation pressure build-up are relatively insensitive to heartwood ratio. The root water uptake curves shift downward as θ increases, but this is simply a geometric effect due to the corresponding decrease in sapwood area. Among the two geometric parameters (R_{tree} and θ) the solution is clearly most sensitive to stem radius, which is fortunate since it is extremely easy to measure (non-destructively).

The two parameters controlling root flux – root area \mathcal{A}_{tree} and reflection coefficient $\mathcal{C}_{r,out}$ – can be estimated from data in the literature, but these still remain the most uncertain parameters in our model. By increasing \mathcal{A}_{tree} over two orders of magnitude, Figure 6c shows that the exudation

pressure exhibits a modest increase; however, over the range [10.4, 18.6] suggested by Day and Harris (2007) there is only a small impact on exudation pressure build-up. The root reflection coefficient has a more conspicuous impact on exudation and Figure 6d shows that the oscillations in pressure trend upwards as $\mathcal{C}_{r,out}$ is reduced. This an obvious consequence of restricting root outflow which retains more water in the xylem that can freeze and subsequently store pressure in the fibers. It is clearly important that we have incorporated the root reflection coefficient in our modified model equations and despite the relative insensitivity to this parameter, there is still an opportunity here for new experiments that aim to obtain better estimates of $\mathcal{C}_{r,out}$ in maple trees.

The final parameter we consider is sap sugar concentration for which Figure 6e shows that increasing γ_s within the range [0.015, 0.04] has the greatest impact on increasing stem pressure compared to the other four parameters. This supports our earlier remarks regarding the essential role played by sugar in terms of generating a local differential between freeze/thaw in fibers and vessels (due to FPD) which permits ice to accumulate in fibers at the same time as the sap in neighboring vessels remains in the liquid state. Increasing γ_s therefore permits additional ice accumulation in fibers through cryostatic suction which is also reflected in a corresponding increase in root water uptake with γ_s . It is worth recalling that sap sugar also induces an osmotic contribution to pressure through Eq. (4), but we have clearly demonstrated in previous work (Graf et al., 2015) that osmosis is eclipsed in importance by the effect of FPD. Finally, because sap sugar content is so easy to measure, it is especially important that any similar experimental study of sap pressure and temperature also includes measurements of γ_s in order that the model can be properly calibrated.

5.3. Multiscale model reproduces realistic exudation behavior

We begin by discussing the results in Figure 7a,b that compare experimental and numerical results for the two red maples R1 and R2. The measurements are dominated by pressure spikes appearing at times $t \approx 13, 15, 16, 18, 22$ days that coincide with similar spikes in simulations. Each spike is clearly matched with a thaw event in which air temperature increases past the melting point. The simulated peak pressure for some spikes does not reach the same peak value as in experiments but the correspondence is nonetheless excellent, not to mention that the pressure minima following subsequent freeze events are captured very closely. The simulations also show that each spike is followed by a relaxation period during which the pressure gradually decays at a rate that is similar to that seen in the measured data.

During the initial 13 days on the other hand, the match between red maple simulations and experiments is not nearly as close. The measured R1 data in Figure 7a shows that the pressure remains essentially constant at zero whereas the simulation exhibits significant pressure fluctuations in response to freeze–thaw events, most notably on days 2 and 9. Deviations are also present with R2, although the match is slightly better because the pressure sensor captures some small fluctuations between days 1–2 and 8–11. One possible explanation for these discrepancies is that the thaw events for times $t < 13$ days are weaker in that temperature increases only slightly above 0°C before either falling below freezing again or hovering near zero, which may be causing the stem to remain more deeply frozen. These “weak thaw” events seem to be captured more readily by the model computations, although the computed pressure does exhibit a more gradual increase instead of the sharp spike seen at the onset of other thaw events; this behavior is especially apparent for the thaw event highlighted in Figure 7a,b during days 9–11.

The observations of low pressure/flow earlier in the season may also be attributed to the fact that trees tend to be very well-buffered to temperature on the north side due to reduced sun exposure (Reid et al., 2020) (recalling that our comparison is based on north-side sensor data). Furthermore,

higher accumulations of snow near the base of the stem may also limit the root water uptake. In either case, it is well known that several repeated cycles of freeze and thaw are typically required before pressure and flow rates can ramp up to higher values.

Next we shift to the comparison depicted in Figure 7c for the sugar maple S1, which shows that the timing of pressure spikes and the subsequent relaxation rate from simulations both exhibit a reasonable match with experiments, although the simulated pressure peak values are significantly lower. We have as yet no definitive explanation for this discrepancy but it may be at least partly due to our pressure average \bar{p} , which is integrated all the way to the heartwood boundary and so includes portions of the xylem that may be more deeply frozen and lower the average. Finally, we single out the thaw event on day 7 during which the simulated pressure builds up much more gradually than in the experimental data, which is again analogous to what we observed for the weak thaw events in trees R1 and R2.

5.4. Essential mechanisms governing sap exudation

These comparisons between experiments and simulations demonstrate that a purely physical model is capable of capturing both qualitatively and quantitatively the essential features of sap transport and pressure generation observed in actual maple trees undergoing exudation. Furthermore, we have clearly identified four mechanisms that are essential for generating stem pressure build-up:

1. The *distinctive cellular structure of maple sapwood* which is made up of libriform fibers containing mostly gas that are connected hydraulically through selectively permeable walls to sap-filled vessels. This structure has two very important consequences: first, it provides a mechanism for fiber–vessel pressure exchange via compression of gas in the fibers; and second, the selectively-permeable nature of the fiber–vessel wall ensures that any liquid drawn into the fiber (through cryostatic suction) contains no sucrose.
2. The *sugar content of sap* in the vessels induces a significant osmotic potential between fiber and vessel, which extends the range of pressures over which gas bubbles persist in sap. However, a much more critical contributor to exudation is the *freezing point depression* (FPD) of roughly 0.16°C in the vessel sap relative to pure water (assuming a 3% sugar content). This is what allows the fibers to accumulate a frozen pure-ice layer while the sugary sap in neighbouring vessels remains thawed because of the FPD.
3. A *clear separation of spatial scales* that exists between freeze–thaw processes on the microscopic (cellular) scale and heat transport on the macroscopic (tree) scale. Specifically, the FPD may appear to be insignificant on the macroscale on which freezing/thawing fronts propagate through the tree stem, but it dominates on the cellular scale by permitting thawed vessels to co-exist adjacent to partially-frozen fibers.
4. An available supply of *soil water in the liquid phase* (even under freezing conditions), combined with the *asymmetry of inflow/outflow in root uptake* (corresponding to reflection coefficient $\mathcal{C}_{r,out} < 1$), which are the key to generating a build-up in exudation pressure over multiple freeze–thaw cycles via accumulation of ice within the fibers. Although this feature is not specific to trees that exude, the availability of significant soil water under sub-zero conditions has recently been confirmed in experiments on maple saplings.

Each of these distinguishing features has been recognized in other studies of maple or related species; however, this is the first time that they have all been linked together to construct a complete explanation for the exudation process that also provides a reasonable match with experimental measurements. This is a minimally complete model in the sense that leaving out any of these four effects from the governing equations results in a failure of the model tree stem to accumulate exudation pressures that are consistent with actual trees. It is important to recognize that these fundamental insights we have gained into the physical mechanisms driving the sap exudation process were only possible by developing a detailed mathematical model and performing careful parametric studies of the resulting numerical simulations.

5.5. Opportunities for future research

This work opens up several opportunities for future research in the study of exudation and sap flow in maple. First of all, we have singled out two parameters for which experimental studies are needed in order to properly calibrate the model and hence obtain more accurate simulation results, namely the root surface area and root reflection coefficient, neither of which has been accurately measured for maple trees.

Our 2D model may be extended in a straightforward fashion to a more realistic 3D axisymmetric stem geometry by stacking a series of 2D cross-sections in the vertical direction and then coupling sap flux and temperature between adjacent sections. We could then incorporate the effects of varying gravitational potential with height, while at the same time obtaining a more realistic representation of how soil water from the roots is drawn by cryostatic suction to higher elevations in the tree. Another important feature that could be easily incorporated into the model equations is the dependence of sap sugar content on height that has been observed by Milburn and Zimmermann (1986). It would then be natural to incorporate the dynamics of the starch conversion process wherein living xylem cells release sugar into the vessels in response to temperature variations (Améglio et al., 2001; Wong et al., 2003). Some authors have also hypothesized that hysteresis and super-cooling effects play a role in the sap exudation process (Charrier et al., 2015; Tyree, 1983; Wu et al., 2017), which would be relatively straightforward to investigate with this model. Finally, there are fascinating connections to explore between sap exudation and freeze-induced embolism, motivated by studies that have demonstrated a close relationship between embolism recovery and positive pressures in xylem (Hölttä et al., 2018; Schenk et al., 2021; Sperry et al., 1988).

Funding

Natural Sciences and Engineering Research Council of Canada (RGPIN-2016-04088 to JMS); Alexander von Humboldt Foundation (Fyodor Lynen Fellowship to IK); North American Maple Syrup Council Research Fund (to JMS); University of Vermont Agricultural Experiment Station (to TRW, TDP, AvdB).

Authors' Contributions

Study conception and design (JMS); algorithm design and implementation (IK, JMS); numerical simulations (MZ, JMS); experimental design and data collection (TRW, TDP, AvdB); data analysis, synthesis and interpretation (MZ, TDP, AvdB, JMS); manuscript writing and revision (all authors).

References

- Allaire G (1992). Homogenization and two-scale convergence. *SIAM Journal on Mathematical Analysis* 23(6):1482–1518.
- Améglio T, Ewers FW, Cochard H, Martignac M, Vandame M, Bodet C, Cruiziat P (2001). Winter stem xylem pressure in walnut trees: effects of carbohydrates, cooling and freezing. *Tree Physiology* 21(6):387–394.
- Baral SK, Berninger F, Schneider R, Pothier D (2017). Effects of heartwood formation on sugar maple (*Acer saccharum* Marshall) discoloured wood proportion. *Trees* 31:105–114.
- Ceseri M, Stockie JM (2013). A mathematical model for sap exudation in maple trees governed by ice melting, gas dissolution and osmosis. *SIAM Journal on Applied Mathematics* 73(2):649–676.
- Ceseri M, Stockie JM (2014). A three-phase free boundary problem involving ice melting and gas dissolution. *European Journal of Applied Mathematics* 25(4):449–480.
- Charrier G, Pramsohler M, Charra-Vaskou K, Saudreau M, Améglio T, Neuner G, Mayr S (2015). Ultrasonic emissions during ice nucleation and propagation in plant xylem. *New Phytologist* 207:570–578.
- Chavarria-Krauser A, Ptashnyk M (2013). Homogenization approach to water transport in plant tissues with periodic microstructures. *Mathematical Modelling of Natural Phenomena* 8(4):80–111.
- Cirelli D, Jagels R, Tyree MT (2008). Toward an improved model of maple sap exudation: the location and role of osmotic barriers in sugar maple, butternut and white birch. *Tree Physiology* 28:1145–1155.
- Cortes PM, Sinclair TR (1985). The role of osmotic potential in spring sap flow of mature sugar maple trees (*Acer saccharum* Marsh.). *Journal of Experimental Botany* 36(1):12–24.
- Dawson TE (1993). Hydraulic lift and water use by plants: implications for water balance, performance and plant-plant interactions. *Oecologia* 95:565–574.
- Day SD, Harris JR (2007). Fertilization of red maple (*Acer rubrum*) and littleleaf linden (*Tilia cordata*) trees at recommended rates does not aid tree establishment. *Arboriculture and Urban Forestry* 33(2):113–121.
- Duchesne I, Vincent M, Wang XA, Ung CH, Swift DE (2016). Wood mechanical properties and discoloured heartwood proportion in sugar maple and yellow birch grown in New Brunswick. *BioResources* 11(1):2007–2019.
- Ewers FW, Améglio T, Cochard H, Beaujard F, Martignac M, Vandame M, Bodet C, Cruiziat P (2001). Seasonal variation in xylem pressure of walnut trees: root and stem pressures. *Tree Physiology* 21:1123–1132.
- Fowler AC, Krantz WB (1994). A generalized secondary frost heave model. *SIAM Journal on Applied Mathematics* 54(6):1650–1675.
- Graf I, Ceseri M, Stockie JM (2015). Multiscale model of a freeze–thaw process for tree sap exudation. *Journal of the Royal Society Interface* 12:20150665.
- Graf I, Stockie JM (2014). A mathematical model for maple sap exudation. *Maple Syrup Digest* 26A(4):15–19.
- Henzler T, Waterhouse RN, Smyth AJ, Carvajal M, Cooke DT, Schäffner AR, Steudle E, Clarkson DT (1999). Diurnal variations in hydraulic conductivity and root pressure can be correlated with the expression of putative aquaporins in the roots of *Lotus japonicus*. *Planta* 210(1):50–60.
- Hölttä T, Dominguez Carrasco MDR, Salmon Y, Aalto J, Vanhatalo A, Bäck J, Lintunen A (2018). Water relations in silver birch during springtime. How is sap pressurized? *Plant Biology* 20:834–847.
- Javot H, Maurel C (2002). The role of aquaporins in root water uptake. *Annals of Botany* 90(3):301–313.
- Johnson LPV (1945). Physiological studies on sap flow in the sugar maple, *Acer saccharum* Marsh. *Canadian Journal of Research C Botanical Sciences* 23:192–197.
- Jones ARC, Alli I (1987). Sap yields, sugar content, and soluble carbohydrates of saps and syrups of some Canadian birch and maple species. *Canadian Journal of Forest Research* 17:263–266.
- Knipfer T, Fricke W (2010). Root pressure and a solute reflection coefficient close to unity exclude a purely apoplastic pathway of radial water transport in barley (*Hordeum vulgare*). *New Phytologist* 187:159–170.
- Konrad I, Peter MA, Stockie JM (2017). A two-scale Stefan problem arising in a model for tree sap exudation. *IMA Journal of Applied Mathematics* 82(4):726–762.
- Larochelle F, Forget E, Rainville A, Bousquet J (1998). Sources of temporal variation in sap sugar content in a mature sugar maple (*Acer saccharum*) plantation. *Forest Ecology and Management* 106:307–313.
- Marvin JW (1949). Changes in bark thickness during sap flow in sugar maples. *Science* 109(2827):231–232.
- Marvin JW (1958). The physiology of maple sap flow. In: Thimann KV, Critchfield WB, Zimmermann MH (Eds.), *The Physiology of Forest Trees: A Symposium Held at the Harvard Forest*. Ronald Press, New York, pp. 95–124.
- Marvin JW (Aug. 20–22, 1968). Physiology of sap production. In: *Sugar Maple Conference*. Michigan Technological University, Houghton, MI, pp. 12–15.
- Marvin JW, Greene MT (Feb. 1959). Some factors affecting the yield from maple tapholes. *Bulletin 611*, Vermont Agricultural Experiment Station, Burlington, VT.
- MATLAB (2020). Version 9.8.0 (R2020a). The MathWorks Inc., Natick, Massachusetts.

- Merwin HE, Lyon H (1909). Sap pressure in the birch stem. *Botanical Gazette* 48(6):442–458.
- Milburn JA, O'Malley PER (1984). Freeze-induced sap absorption in *Acer pseudoplatanus*: a possible mechanism. *Canadian Journal of Botany* 62(10):2101–2106.
- Milburn JA, Zimmermann MH (1986). Sapflow in the sugar maple in the leafless state. *Journal of Plant Physiology* 124:331–344.
- O'Leary JW (1965). Root-pressure exudation in woody plants. *Botanical Gazette* 126(2):108–115.
- Perkins TD, van den Berg AK (2009). Maple syrup—Production, composition, chemistry, and sensory characteristics. In: Taylor SL (Ed.), *Advances in Food and Nutrition Research*. Vol. 56. Elsevier, Ch. 4, pp. 101–143.
- Reid S, Driller T, Watson M (2020). A two-dimensional heat transfer model for predicting freeze–thaw events in sugar maple trees. *Agricultural and Forest Meteorology* 294:108139.
- Robitaille G, Boutin R, Lachance D (1995). Effects of soil freezing stress on sap flow and sugar content of mature sugar maples (*Acer saccharum*). *Canadian Journal of Forest Research* 25(4):577–587.
- Sachs J (1860). Quellungserscheinungen an Hölzern. *Botanische Zeitung* 18(29):253–259.
- Schenk HJ, Jansen S, Hölttä T (2021). Positive pressure in xylem and its role in hydraulic function. *New Phytologist* 230:27–45.
- Sorkin L (Jan. 20, 2014). Maple syrup revolution: A new discovery could change the business forever. *Modern Farmer*, URL <http://modernfarmer.com/2014/01/maple-syrup-revolution>.
- Sperry JS, Donnelly JR, Tyree MT (1988). Seasonal occurrence of xylem embolism in sugar maple (*Acer saccharum*). *American Journal of Botany* 75(8):1212–1218.
- Steudle E (1994). Water transport across roots. *Plant and Soil* 167:79–90.
- Steudle E, Peterson CA (1998). How does water get through roots? *Journal of Experimental Biology* 49(322):775–788.
- Stevens CL, Eggert RL (1945). Observations on the causes of the flow of sap in red maple. *Plant Physiology* 20:636–648.
- Tyree MT (1983). Maple sap uptake, exudation, and pressure changes correlated with freezing exotherms and thawing endotherms. *Plant Physiology* 73:277–285.
- Tyree MT (April 10–12, 1995). The mechanism of maple sap exudation. In: Terazawa M, McLeod CA, Tamai Y (Eds.), *Tree Sap: Proceedings of the First International Symposium on Sap Utilization*. Hokkaido University Press, Bifuka, Japan, pp. 37–45.
- Tyree MT, Yang S, Cruiziat P, Sinclair B (1994). Novel methods of measuring hydraulic conductivity of tree root systems and interpretation using AMAIZED: A maize-root dynamic model for water and solute transport. *Plant Physiology* 104:189–199.
- Tyree MT, Zimmermann MH (2002). *Xylem Structure and the Ascent of Sap*, 2nd Edition. Springer Series in Wood Science. Springer-Verlag, Berlin.
- Visintin A (1996). Models of Phase Transitions. Vol. 28 of *Progress in Nonlinear Differential Equations and Their Applications*. Birkhäuser, Boston.
- Wiegand KM (1906). Pressure and flow of sap in wood. *The American Naturalist* 40(474):409–453.
- Wilmot T (2006). Temperatures in the sugarbush. *Maple Syrup Digest* 18A(2):20–23.
- Wong BL, Baggett KL, Rye AH (2003). Seasonal patterns of reserve and soluble carbohydrates in mature sugar maple (*Acer saccharum*). *Canadian Journal of Botany* 81:780–788.
- Wu D, Zhou X, Jiang X (2017). Water and salt migration with phase change in saline soil during freezing and thawing processes. *Groundwater* 56(5):742–752.
- Yang S, Tyree MT (1992). A theoretical model of hydraulic conductivity recovery from embolism with comparison to experimental data on *Acer saccharum*. *Plant, Cell & Environment* 15:633–643.
- Zarrinderakht M (Mar. 2017). Numerical simulations of a multiscale model for maple sap exudation. Master's thesis, Department of Mathematics, Simon Fraser University, Burnaby, BC, Canada. URL <https://theses.lib.sfu.ca/thesis/etd10022>.